

Flow dynamics of shear-coaxial cryogenic nitrogen jets under supercritical conditions with and without acoustic excitations

Cite as: Phys. Fluids **33**, 076111 (2021); <https://doi.org/10.1063/5.0054435>

Submitted: 18 April 2021 . Accepted: 22 June 2021 . Published Online: 16 July 2021

Tao Liu,  Xingjian Wang, and  Vigor Yang

COLLECTIONS

Paper published as part of the special topic on [Tribute to Frank M. White on his 88th Anniversary](#)



View Online



Export Citation



CrossMark

ARTICLES YOU MAY BE INTERESTED IN

[Interaction of ocean wave with a harbor covered by an ice sheet](#)

Physics of Fluids **33**, 057109 (2021); <https://doi.org/10.1063/5.0051376>

[Some general solutions for linear Bragg–Hawthorne equation](#)

Physics of Fluids **33**, 077113 (2021); <https://doi.org/10.1063/5.0055228>

[Energy stable modeling of two-phase flow in porous media with fluid–fluid friction force using a Maxwell–Stefan–Darcy approach](#)

Physics of Fluids **33**, 073312 (2021); <https://doi.org/10.1063/5.0053373>

Physics of Fluids

SPECIAL TOPIC: Flow and Acoustics of Unmanned Vehicles

Submit Today!



Flow dynamics of shear-coaxial cryogenic nitrogen jets under supercritical conditions with and without acoustic excitations

Cite as: Phys. Fluids **33**, 076111 (2021); doi: [10.1063/5.0054435](https://doi.org/10.1063/5.0054435)

Submitted: 18 April 2021 · Accepted: 22 June 2021 ·

Published Online: 16 July 2021



View Online



Export Citation



CrossMark

Tao Liu,¹ Xingjian Wang,^{2,a),b)}  and Vigor Yang^{3,a)} 

AFFILIATIONS

¹Department of Mechanical and Nuclear Engineering, The Pennsylvania State University, University Park, Pennsylvania 16802, USA

²Department of Mechanical and Civil Engineering, Florida Institute of Technology, Melbourne, Florida 32901, USA

³School of Aerospace Engineering, Georgia Institute of Technology, Atlanta, Georgia 30332, USA

Note: This paper is part of the special topic, Tribute to Frank M. White on his 88th Anniversary.

^{a)}Authors to whom correspondence should be addressed: xingjianwang@tsinghua.edu.cn and vigor.yang@aerospace.gatech.edu

^{b)}Present address: Department of Energy and Power Engineering, Tsinghua University, Beijing 10084, China.

ABSTRACT

The three-dimensional flow structures and dynamics of shear-coaxial nitrogen jets under supercritical conditions are comprehensively investigated using the large-eddy simulation technique. The theoretical framework is based on the full conservation laws and accommodates real-fluid thermodynamics and transport theories over the entire range of fluid states. Cryogenic liquid nitrogen (132 K) is delivered through the inner tube of a shear-coaxial nozzle, and gaseous nitrogen (191 K) is injected through the outer annulus, into a high-pressure environment at 233 K. Particular attention is paid to the influence of operating parameters on the flow evolution of the coaxial jets. Two supercritical pressure conditions, 4.94 and 10.0 MPa, and three outer-to-inner velocity ratios in the range of 2.03–3.75, are considered. Results reveal that the flowfield downstream of the coaxial jets is characterized by two potential cores and three shear layers. Two counter-rotating recirculation zones are formed next to the central post-tip. The characteristic frequencies of flow recirculation and shear-layer instability are analyzed using power spectral analysis. Increasing the pressure and the velocity ratio enhances turbulent mixing, promotes the entrainment of the outer stream into the inner region, and advances the pinching point of vortical motion to the centerline, thereby leading to a decreased length of the inner dark core. The predicted dark core length and outer spreading angle show good agreement with experimental results. The introduction of transverse acoustic excitation induces large sinusoidal oscillations of the inner dense-fluid stream along the direction of acoustic motion and promotes the mixing of the inner and outer streams.

Published under an exclusive license by AIP Publishing. <https://doi.org/10.1063/5.0054435>

I. INTRODUCTION

The design of an injector has significant influence on the fuel/oxidizer mixing characteristics, combustion stability behavior, faceplate thermal protection, and transient performance of an energy conversion system.¹ Shear-coaxial injectors, in particular, have proven to be well suited for use in cryogenic liquid rocket engines, such as the space shuttle main engine (SSME), the Ariane 5 Vulcain engine, and the RL-10 and J-2 rocket engines. The working fluids involved in these applications are injected, often in a cryogenic state, into an environment with pressure exceeding their thermodynamic critical value, rendering supercritical fluid behavior. In a typical liquid-oxygen/hydrogen (LOX/H₂) coaxial injector, for example, the center oxygen jet is injected at subcritical temperature while the hydrogen is injected

through a coaxial annulus at supercritical temperature, after being heated in the cooling system.² The center stream undergoes a trans-critical change of thermodynamic state as it mixes with the annular jet downstream of the injector. This type of mixing process presents characteristics that are distinct from those of classical liquid jet atomization and mixing and are still not well documented for supercritical pressures.³ This paper investigates the flow dynamics of shear-coaxial injectors with and without acoustic excitation at supercritical pressure, typical of contemporary propulsion and power-generation systems such as liquid-fuel rocket, diesel, and gas-turbine engines. Emphasis is put on the effect of operating conditions, including chamber pressure and velocity ratio, on the mixing efficiency, and the effect of transverse acoustic modulation on jet dynamics.

Earlier studies, both experiments^{4–8} and numerical simulations,^{9–12} revolved around supercritical single jet dynamics. Emphasis was placed on the interfacial flow structures and evolution of the liquid potential core and jet spreading under various operation conditions. Oschwald and Schik⁴ employed spontaneous Raman scattering to determine the temperature and density distribution of cryogenic nitrogen jets into a supercritical nitrogen environment. Chehroudi *et al.*⁶ conducted a series of experiments on the injection of cryogenic liquid jets into an environment of supercritical temperature and pressure that was varied from subcritical to supercritical. Flow visualization was performed using back-illuminated images. At subcritical pressure, the jets showed the classical atomization process with surface irregularities and small droplet formation. At supercritical pressure, the jets behaved like turbulent gaseous jets with no detectable droplets, and the jet growth rate measurements agreed quantitatively with the theory of incompressible but variable-density mixing layers. Branam and Mayer⁷ examined density profiles, turbulent length scales, and spreading angles of cryogenic nitrogen injection between Raman and shadowgraph images and computational models. The result provided insight into mass mixing and jet dissipation. Good agreement on jet-spreading angle was achieved among different measurement methods and empirical models. Segal and Polikhov⁸ studied the dynamics of liquid jet breakup under subcritical and supercritical pressures using planar laser-induced fluorescence (PLIF), which captured previously undetected liquid jet core structures. Subcritical jet breakup features ligament and droplet formation due to ambient gas inertia and surface tension forces, while in supercritical jet breakup, with reduced surface tension, the liquid–gas interface is smooth and ligaments are not observed. Linear jet stability analysis showed good agreement with experimental results under subcritical pressure but failed to predict transcritical and supercritical results. Muthukumaran and Vaidyanathan¹³ implemented PLIF to study elliptical jet dynamics, with nitrogen and helium as working fluids. DeSouza and Segal¹⁴ recently compared the shadowgraph and PLIF techniques for flow visualization of cryogenic injection at subcritical and supercritical pressures. The PLIF results provided quantitative measurement of central jet plane density and density gradients.

In studies of shear-coaxial injectors, Mayer and colleagues^{15,16} were among the first to experimentally identify the differences in flow structures between subcritical and supercritical mixing. They examined the flow and flame structures of liquid oxygen (LOX) and gaseous hydrogen in a shear-coaxial injector with the operating pressure up to 10 MPa using the shadowgraph technique. The visualized flowfield showed that thread- or string-like structures appear in the LOX stream when the chamber pressure exceeds 4.5 MPa. Candel *et al.*¹⁷ imaged LOX/H₂ jet flames in a shear-coaxial injector using various optical methods, including light emission from OH radicals, laser-induced fluorescence of OH and O₂, and Raman scattering. The OH images provided useful information on flame stabilization mechanisms. Extended efforts were later made on the LOX/methane flames in shear-coaxial injectors under both transcritical and supercritical conditions.^{18–21} The images provided guidance for the design of numerical modeling tools. Candel *et al.*¹⁹ found that the controlling mechanism of flame evolution is different for subcritical and supercritical pressures because the relevant characteristic time scales are different. At subcritical pressure, the processes of atomization and evaporation are most time-consuming and thus determine the rates of combustion and

flame length. At supercritical pressure, mass transfer between dense fluid and its surrounding is the rate-controlling process, due to the diminishing of surface tension and latent heat.

Davis and Chehroudi^{1,22,23} studied the dynamic response of a shear-coaxial jet at different pressures in an externally imposed acoustic field. Liquid nitrogen (LN₂) was injected into the center with an outer gaseous nitrogen (GN₂) jet in the annular region. They argued that the outer GN₂ jet played two key roles: (1) promoting heat exchange with the inner jet and (2) assisting inner jet breakup at subcritical pressure and enhancing mixing at supercritical pressure. The dark core length showed different dependence on momentum flux ratio (M), with a $M^{-0.2}$ dependence at subcritical pressure and a $M^{-0.5}$ dependence at near-critical and supercritical pressures. The dark core length decreases as the chamber pressure increases from subcritical to supercritical pressures. Large-scale sinusoidal structures along the dark core were observed when the external acoustic field was turned on.

High-fidelity numerical simulations can provide additional insight into flow structures and dynamic characteristics, especially in the injector near-field region under extreme operating conditions, where optical diagnostics are very challenging. Oefelein^{24,25} explored the thermophysical characteristics of shear-coaxial LOX–H₂ flames at supercritical pressure and found that the flame was diffusion-dominated and exceedingly large thermodynamic property gradients were present. Zong and Yang²⁶ used large-eddy simulations (LES) to examine the near-field flow and flame dynamics of a LOX–methane shear-coaxial injector at supercritical pressure. The flowfield was characterized by three mixing layers from the trailing edges of the two concentric tubes, and the diffusion-dominated flame was found to anchor in the wake region of the LOX post. The anchoring mechanism was consistent with experimental findings.^{19,21} The higher momentum flux ratio of this injector enhanced mixing and shortened the dark cores of both the LOX and methane jets. Other numerical studies have been conducted to explore the dynamics of LOX/methane flames in shear-coaxial injectors under practical operating conditions typical of liquid rocket engines with or without acoustic excitation.^{27–32} Schmitt *et al.*³³ used a combination of experiments and numerical simulations to explore the effects of injector geometry and operating parameters on the LN₂/GN₂ mixing process at supercritical pressures. When the momentum flux ratio exceeded a critical value, the dark core was abruptly terminated shortly downstream of the injector exit, where a recirculation region formed. External acoustic modulation was also examined, with in-phase and out-of-phase radial perturbations.

In spite of recent advances in numerical modeling of supercritical flow physics and combustion dynamics,^{3,34–40} there remain many physical problems to be studied, especially with geometries for engineering applications. The present work focuses on high-fidelity simulations of the flow physics of a shear-coaxial injector with cryogenic and gaseous nitrogen injection at supercritical pressure, under conditions with and without acoustic excitations. The series of simulations presented here are validated against experiments conducted by Chehroudi and co-workers.^{23,41} Results provide detailed information about flow structures and dynamics in the injector near field. Building on the preliminary results presented previously,⁴² various operating conditions, including chamber pressure, velocity ratio, and transverse acoustic modulation, are examined in detail.

The paper is organized as follows. Section II briefly introduces the theoretical formulation and numerical framework. Section III

describes the computational setup and boundary conditions. Detailed flow dynamics are discussed in Sec. IV, and the work is summarized and concluded in Sec. V.

II. THEORETICAL AND NUMERICAL FORMULATION

The theoretical foundation of the present study is well documented in Refs. 3, 40, and 43, which deal with supercritical fluid flows and combustion over the entire range of fluid thermodynamic states. Turbulence closure is achieved using the LES technique, in which large-scale turbulent eddies are numerically resolved and small, subgrid-scale motions are modeled. A compressible version of the Smagorinsky model is employed to characterize the effects of subgrid-scale (sgs) motion.⁴⁴ The governing equations for LES are written as follows:

$$\frac{\partial \bar{\rho}}{\partial t} + \frac{\partial \bar{\rho} \tilde{u}_j}{\partial x_j} = 0, \tag{1}$$

$$\frac{\partial \bar{\rho} \tilde{u}_i}{\partial t} + \frac{\partial (\bar{\rho} \tilde{u}_i \tilde{u}_j + \bar{p} \delta_{ij})}{\partial x_j} = \frac{\partial (\bar{\tau}_{ij} - \tau_{ij}^{sgs})}{\partial x_j}, \tag{2}$$

$$\frac{\partial \bar{\rho} \tilde{e}_t}{\partial t} + \frac{\partial [\bar{\rho} \tilde{e}_t + \bar{p}] \tilde{u}_j}{\partial x_j} = \frac{\partial [\tilde{u}_i \tau_{ij} + \sigma_{ij}^{sgs} + \bar{q}_j - q_j^{sgs} - H_j^{sgs}]}{\partial x_j}. \tag{3}$$

Here unclosed sgs terms include shear stresses (τ_{ij}^{sgs}), viscous work (σ_{ij}^{sgs}), heat flux (q_j^{sgs}), and energy flux (H_j^{sgs}). Detailed implementation of sgs models may be referred to Refs. 40 and 42.

Thermodynamic properties, including density, enthalpy, and specific heat at constant pressure, are evaluated according to fundamental thermodynamics theories and a modified Soave–Redlich–Kwong equation of state.⁴⁵ It should be noted that the sgs terms in the filtered equation of state may become significant for supercritical and trans-critical fluid flows, compared to other filtered terms.^{40,46} Yet the sgs contributions are often neglected in the filtered equation of state since no robust model is currently available. Transport properties, including thermal conductivity and dynamic viscosity, are estimated using extended corresponding-state principles. Mass diffusivity is obtained by the Takahashi method calibrated for high-pressure conditions.⁴⁷ The evaluation of thermodynamic and transport properties has been validated and implemented in previous studies.³

There are many numerical challenges in solving supercritical fluid flows. For example, thermodynamic nonidealities and transport anomalies take place as the fluid transits from subcritical to supercritical conditions. Treating these abnormal changes in a manner consistent with the intrinsic characteristics of the numerical algorithm presents a major obstacle. In addition, the rapid variation of the fluid state, and a wide range of length and time scales in high-pressure, low Mach-number flows pose the well-known stiffness problem.⁴⁸ To this end, the numerical framework was established by implementing a preconditioning scheme and a unified treatment of general-fluid thermodynamics.⁴⁸ The framework employs a density-based, finite-volume methodology, along with a dual-time step integration technique.²⁶ Temporal discretization is fulfilled using a second-order backward difference scheme, and the inner-loop pseudo-time term is integrated with a four-step Runge–Kutta scheme. Spatial discretization is obtained using a fourth-order central difference scheme in generalized coordinates. Fourth-order matrix dissipation is implemented to ensure

numerical stability and minimum contamination of the solution.⁴⁹ Finally, a multiblock domain decomposition technique associated with the message passing interface technique for parallel computing is applied to optimize computational speed.

III. COMPUTATIONAL SETUP AND BOUNDARY CONDITIONS

Figure 1 shows a schematic of the shear-coaxial injector used in the experiment,^{23,33} including the computational domain considered in this work. Cryogenic liquid nitrogen is delivered through the inner cylindrical tube, acting as oxidizer, and gaseous nitrogen (GN_2) is injected into the coaxial annulus at a higher velocity, acting as fuel. The injector has a post-thickness δ of 0.541 mm with zero post-recess. The inner diameter d_i is 0.508 mm and the outer surface diameter of the coaxial annulus d_o is 2.42 mm. The computational domain covers $2 d_i$ axially inside the shear-coaxial injector and spans $60 d_i$ and $12 d_i$ downstream of the injector exit in the axial and radial directions, respectively.

A variety of operating conditions, including ambient pressure, velocity ratio, and acoustic modulation, are investigated. Numerical simulations are conducted for a total of five cases. Table I lists the inflow boundary conditions and initial conditions. The inlet temperatures for inner and out jets are fixed for all cases. Two ambient pressures are considered. Cases 1, 3, and 5 have an ambient pressure of 4.94 MPa, and cases 2 and 4 have an ambient pressure of 10 MPa. For comparison, case 1 is treated as the baseline, where the ambient pressure and velocity ratio are the same as those of experiments.^{22,23} The jet velocities in the present study are higher than those in experiments in order to shorten the computational time. Inflow velocities are carefully selected to match the momentum flux ratio of practical engines. In particular, cases 1 and 4 have a momentum flux ratio of approximately 3.45, similar to that of the SSME preburner injector. The momentum flux ratio in case 2 is similar to that of the SSME main chamber injector. The velocity ratio varies from 2.03 to 3.75 through

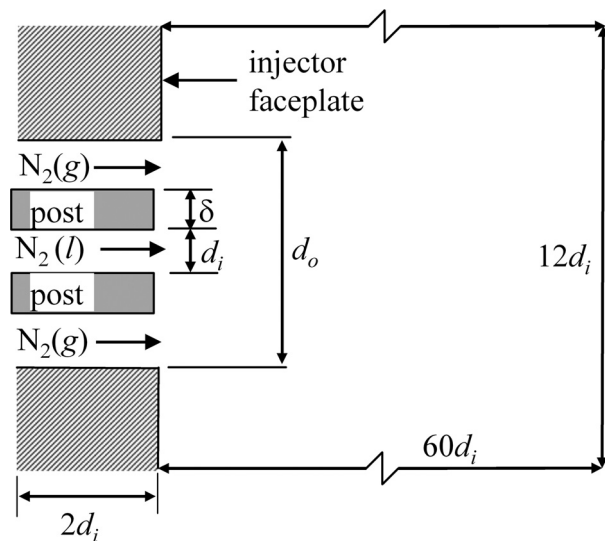


FIG. 1. Schematic of the shear-coaxial injector employed in the present study (subscripts: o—outer; i—inner).

TABLE I. Inflow and initial conditions for all cases (subscripts: *o*—outer; *i*—inner; *a*—ambient).

	Case 1/5	Case 2	Case 3	Case 4
P_a (MPa)	4.94	10	4.94	10
T_a (K)	233	233	233	233
T_o (K)	191	191	191	191
T_i (K)	132	132	132	132
ρ_o (kg/m ³)	98.8	217.2	98.8	217.2
ρ_i (kg/m ³)	404.0	555.4	404.0	555.4
u_o (m/s)	120	120	65	95
u_i (m/s)	32	32	32	32
u_o/u_i	3.75	3.75	2.03	2.97
$(\rho u)_o/(\rho u)_i$	0.92	1.47	0.50	1.16
$(\rho u^2)_o/(\rho u^2)_i$	3.44	5.50	1.01	3.45
Re_o (10 ⁵)	3.3	5.8	1.8	4.6
Re_i (10 ⁵)	1.3	1.0	1.3	1.0
At	0.607	0.438	0.607	0.438

changes in the inlet velocity of the coaxial GN₂ jet. Table I also provides the Reynolds numbers based on the flow parameters of the inner and outer tubes and the Atwood number. Cases 1–4 are setup with acoustic modulation off, while case 5 has the same flow conditions as case 1, but has the acoustic modulation turned on.

A grid system of 301 × 141 × 81 (3.44 × 10⁶ total) points is adopted along the axial, radial, and azimuthal directions, respectively. More than 30 grid points are used along the radial direction for each inlet section to guarantee the conservation of flow properties. The grid resolution is chosen based on the inlet Reynolds number, such that the largest grid size falls in the inertial subrange of the turbulent energy spectrum.

At the inlet boundary, both the velocity and temperature are specified, and the pressure is obtained from a simplified one-dimensional axial-momentum equation. No artificial turbulence intensity is provided at the inlet section because the strong shear layers and high-intensity turbulence generated in the flowfield will overshadow the influence of the incoming turbulence. At the downstream boundaries in both the axial and radial directions, the ambient pressure is specified, with all other primary unknown flow variables extrapolated from the interior. The nonslip, adiabatic boundary conditions are applied to all solid walls. For the study of acoustic modulation on the shear-coaxial jet dynamics, periodic pressure oscillations are imposed at the radial outflow boundaries to generate transverse standing acoustic waves in the injector downstream region.

IV. RESULTS AND DISCUSSION

In this section, the results of simulation of cryogenic LN₂/GN₂ shear-coaxial injection for all cases are presented. Effects of operating chamber characteristics, velocity ratio, and acoustic modulation are explored in detail and compared to experimental data from the literature. For each case, the calculation is performed over an extended period of time to ensure the establishment of a fully developed flowfield. Simulation is then continued for about six flow-through times to obtain statistically meaningful data.

Figure 2 shows the density and constant-pressure specific heat of nitrogen under the operating conditions considered here. The critical temperature and pressure of nitrogen are 126 K and 3.40 MPa, respectively. There is discontinuity of thermodynamic properties across the phase-change point at subcritical pressure (0.1 MPa), while a smooth transition from compressed liquid to supercritical fluid occurs at supercritical pressure (4.94 and 10.0 MPa). This transition features a large property change with an inflection point, where the density gradient with respect to temperature is the largest and the constant-pressure specific heat reaches the maximum value. The inflection point is also known as the pseudo-boiling point.⁵⁰ In the present study, the flowfield temperature ranges from 132 to 233 K and the lower bound is below the inflection-point temperature for both 4.94 and 10 MPa. It is expected that strong density stratification and the rapidly increasing specific heat in the transition region will influence flow dynamics significantly.

A. Instantaneous flowfield

In this subsection, the instantaneous distributions of various flow properties are presented, along with a general schematic of the flow

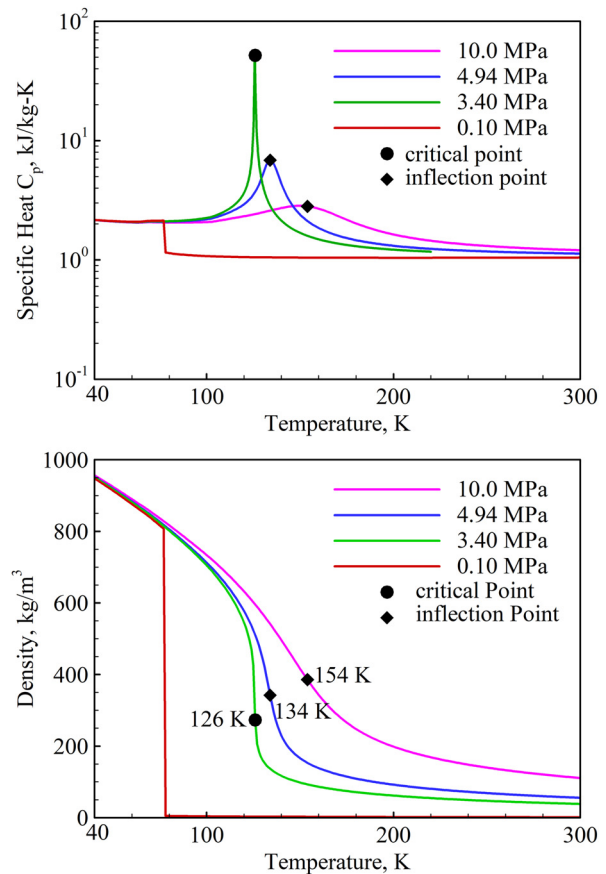


FIG. 2. Profiles of density and constant-pressure specific heat of nitrogen as a function of temperature at different pressures.

pattern. The evolution of the dark cores and shear layers in different cases is discussed.

Figure 3 shows instantaneous distributions of temperature, density, compressibility factor, vorticity magnitude, and temperature-gradient magnitude in case 3 with ambient pressure of 4.94 MPa and outer-to-inner velocity ratio of 2.03. The initial ambient temperature is 233 K. Real-fluid behaviors are observed immediately downstream of the injector exit. The compressibility factor varies widely from 0.36 (liquid-like) to nearly unity (gas-like) in a short radial span. This accompanies the large radial density change from 365 kg/m³ on the centerline to 75 kg/m³ in the outer freestream region. Vorticity is dynamically distributed around the two shear-coaxial injection exits. The overall flowfield of the shear-coaxial jet is characterized by three shear layers and two potential cores. The inner potential core is known as the dark core and features the largest density in the flowfield. This pattern is schematically illustrated in Fig. 4. The three shear layers originate from the wall boundary layers in the center tube and inner and outer surfaces of the coaxial annulus, which detach from the rims and produce vorticity roll-up at the boundary of potential cores. The inner shear layer surrounds the dark core of the central jet, and it merges with the middle shear layer in the wake region of the LN₂ post. The outer shear layer occurs at the boundary between the GN₂ jet and the ambient fluid.

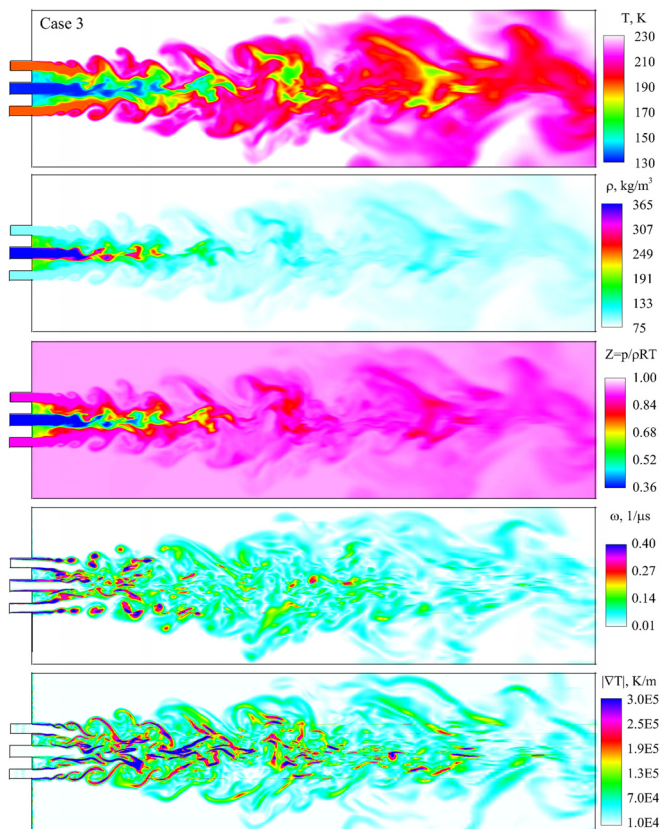


FIG. 3. Instantaneous distributions of (top to bottom) temperature, density, compressibility factor, vorticity magnitude, and temperature-gradient magnitude in case 3 ($\rho = 4.94$ MPa).

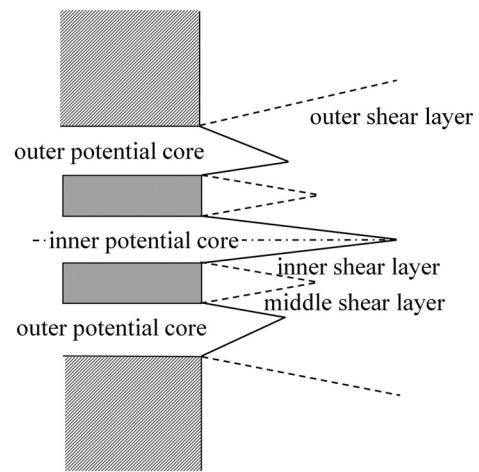


FIG. 4. Schematic diagram of flow pattern in injector near field.

Also shown in Fig. 3, large density- and temperature-gradient regions are formed around the central liquid jet surface and corrugated by the evolution of the inner shear layer. An earlier study indicated that the occurrence of the large density-gradient regions significantly influences the single jet dynamics by amplifying the axial flow oscillations and damping the radial ones.¹⁰ It is thus expected the effect of density stratification on the shear-coaxial jet dynamics. Because of the rapid variation of the compressibility factor, the density undergoes faster variation than temperature downstream of the inner potential core. Unsteadiness occurs due to convective instability in the shear layers, resulting in the development of large-scale coherent vortex structures. The evolution and interaction of large coherent structures facilitate the mixing and entrainment of ambient warmer fluid into the inner cold fluid, along with a series of thread-like entities emerging from the jet surface. Consistent with experimental observations,²⁵ the evolution of the outer shear layers then prevails over the development of the inner layers because of the greater velocity difference between the annulus GN₂ stream and the surroundings, as manifested by the large vorticity magnitude in the outer shear layer. The inner shear layer, on the other hand, exhibits the largest density gradient and the smallest shear force. The middle and outer shear layers separated by the annulus port merge together after large-scale vortices grow up and become a single outer shear layer. With the continuous growth further downstream, the large-scale vortices reach the centerline, mix with the inner jet, and truncate the inner jet, resulting in the formation of the so-called inner potential core. This pattern of flow evolution is further illustrated in the isosurfaces of instantaneous temperature, as shown in Fig. 5. The inner cold dense core fades away after a short flow path when the large-scale vortices from the outer shear layers pinch the centerline. The annular warm jet fades after a long flow path and full mixing with the ambient fluid.

Figure 6 shows a comparison of instantaneous distributions of temperature and compressibility factor for cases 1–4. Cases 1 and 3 have an ambient pressure of 4.94 MPa, while cases 2 and 4 have an ambient pressure of 10.0 MPa. The compressibility factor in the inner dark core decreases with increasing ambient pressure. At the same

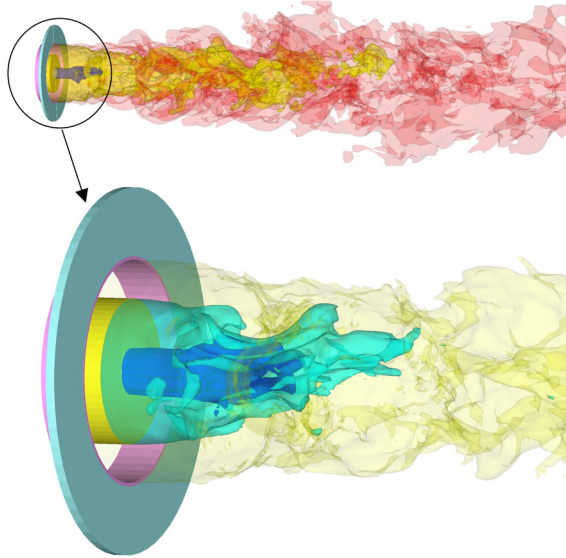


FIG. 5. Global and zoomed-in views of isosurfaces of temperature at four different values (blue: 134 K; cyan: 152 K; yellow: 192 K; red: 215 K) in case 1.

ambient pressure, the length of the inner potential core is shorter for the cases with a higher velocity ratio. This phenomenon can be attributed to the enhanced turbulent mixing at a higher velocity ratio. According to a linear stability analysis on real-fluid mixing layers,⁴²

the amplification rates of mixing layers increase with shear magnitude. Because of the fast growth in the length scales of the vortex structure, the large-scale vortices pinch the centerline earlier and the potential cores of the inner streams are reduced.

Distribution of Q-criterion is a good way to illustrate the flow coherent vortices. Figure 7 shows the isosurface of positive Q with and without the regions outside the inner tube in case 3. The definition of Q is given by

$$Q = \frac{(\Omega_{ij}\Omega_{ji} - S_{ij}S_{ji})}{2}, \tag{4}$$

where $\Omega_{ij} = (\partial u_i / \partial x_j - \partial u_j / \partial x_i) / 2$ denotes rotation and $S_{ij} = (\partial u_i / \partial x_j + \partial u_j / \partial x_i) / 2$ denotes strain. The isosurface of positive Q separates the areas where the strength of rotation overcomes the strength of strain, making those surfaces eligible as vortex envelopes.⁵¹ Large-scale helical structures and discrete vortex rings form intermittently in the near field of the outer shear layer. These rings seem to have the same wavelength and decay in the downstream region. The dominance of helical instability implies that numerical simulations based on cylindrical sectors with periodic boundaries may be inadequate to reliably model the mixing physics. Similar structures develop behind the annular gap between the outer and inner shear layers, representing the locations of recirculation bubbles. In the inner shear layer, the helical structures span a shorter distance downstream of the injector exit. This may be explained by the fact that the entrainment of the outer jet is so fast that it destroys the large structures originating from the inner tube edge with earlier onset of secondary instabilities.

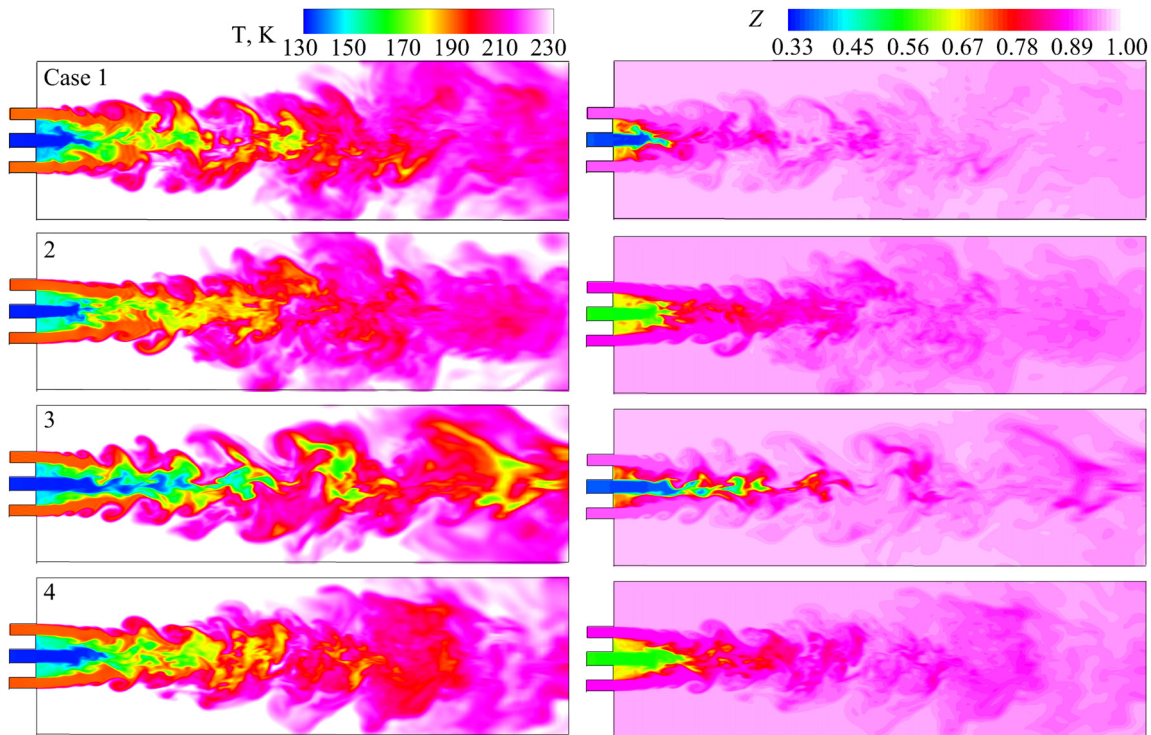


FIG. 6. Instantaneous distributions of temperature and compressibility factor in cases 1–4.

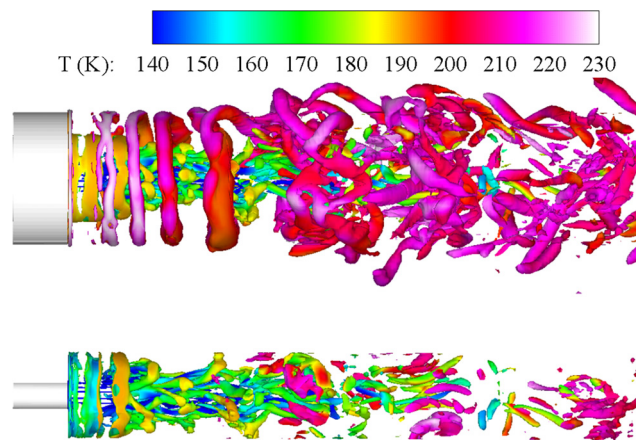


FIG. 7. Isosurfaces of instantaneous Q ($=10^9 \text{ s}^{-2}$) colored by the temperature field (top: complete, bottom: only inner jet).

The aspect ratio, defined as the ratio of the jet radius to the momentum thickness of the shear layer, is found to play an important role in determining the azimuthal wave numbers of secondary instabilities.⁵² The aspect ratios at the injector exit are estimated for both the inner and outer tubes. The minimum aspect ratios are 11.0 and 10.4 for the inner and outer tubes, respectively. They both occur in case 2. Their counterparts for case 3 are 14.7 and 16.4, respectively. The helical mode $m=1$ occurs immediately downstream of the injector exit for both the inner and outer tubes, as manifested in Fig. 7. The core-centered elliptical-type secondary instability is shown in Fig. 6. Further downstream, hyperbolic-type instability takes place and turns the helical structures to more complex three-dimensional structures, since perturbations with higher azimuthal wave numbers become important. These observations are consistent with linear stability theories of three-dimensional round jets⁵² and plane mixing layers.⁵³ It would be interesting in the future to explore the roles of higher wavenumbers in complex turbulent structures future downstream.

B. Mean flowfield

In this subsection, the mean flow field is presented to reveal the overall flow structures and distributions of flow properties. The mean flow properties are obtained by averaging flow snapshots collected over six flow-through times. The spatial-averaging procedure is useful to further transform the mean flow data from high-dimensional space to low dimensional space, for better visualization and comparison with experiments.

Figure 8 shows the isosurfaces of the mean pressure and temperature fields. The streamlines based on the mean axial and radial velocities on a sectional plane crossing the jet centerline are also shown. Flow recirculation zones consistent with those found in experiments^{19,23} are observed just behind the LN₂ post-tip, enveloped by a low-pressure region. The two counter-rotating zones separate the inner and outer potential cores, which merge at the end of the recirculation zone. Rehab *et al.*⁵⁴ discussed the mechanism responsible for the occurrence of the recirculating regime in an incompressible shear-coaxial jet with zero post-thickness. When the jet velocity ratio increases to a limit value, the dynamic pressure decreases until it is

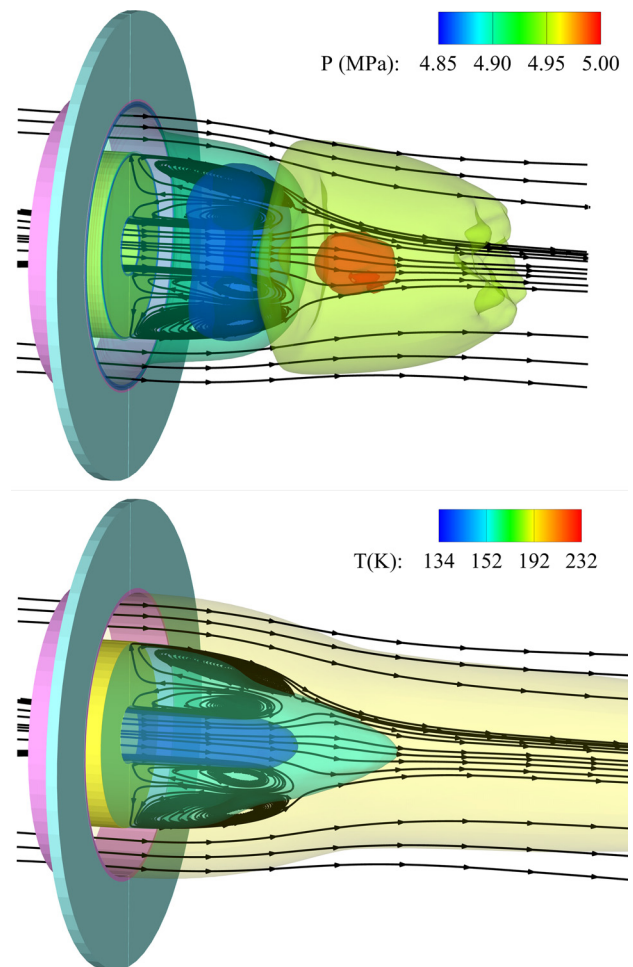


FIG. 8. Isosurfaces of mean pressure and temperature fields in case 3.

insufficient to accelerate the flow in the positive direction, and the flow reverses. Although the velocity ratios in this work are much lower than their predicted values, a recirculation zone still occurs because of the real-fluid effects and finite post-thickness. Please note that in Rehab *et al.*⁵⁴ the inner tube was infinitely thin and the recirculation bubble appeared on the jet axis. In the present analysis, with a more realistic inner tube, the wake region behind the LN₂ post can easily generate flow reversal attaching to the post-tip.

Figure 9 shows the azimuthally averaged distributions of mean temperature and axial velocity in cases 1–4. The central dark core is clearly visualized (left) in blue. Three operating parameters, ambient pressure, velocity ratio, and momentum flux ratio, have been shown to be important in the evolution of the dark core.^{23,33,41} Higher ambient pressure or momentum flux ratio tends to induce a shorter dark core. This is evidenced by several observations in Fig. 9. Having the same momentum flux ratio as case 4, case 1 presents a longer cryogenic region, with higher ambient pressure. The dark core in case 3 is the longest among the cases, mainly due to its lower ambient pressure,

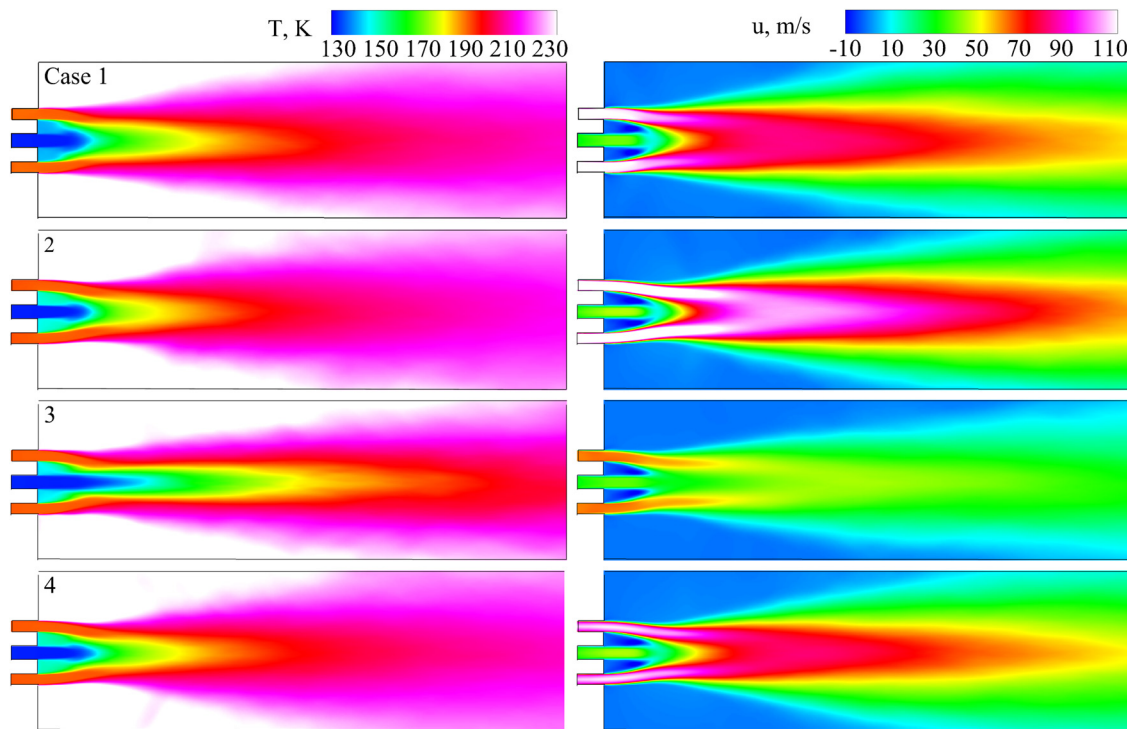


FIG. 9. Azimuthally averaged distributions of mean temperature and axial velocity in cases 1–4.

velocity ratio, and momentum flux ratio. The negative axial velocity zone implies the existence of a flow recirculation region immediately behind the post-tip. The size of the recirculation region is roughly the same for all cases.

Figure 10 presents the mean temperature distributions in the radial direction from the present LES calculations, the Reynolds-Averaged Navier-Stokes (RANS)/LES calculations,⁵⁵ and experimental measurements (D10–D12).²³ The data were collected at a specific axial location ($0.28 d_i$) where the temperature measurements are taken. The operating conditions related to this figure are summarized in Table II. Case 1 has the same pressure and temperature as Experiment D12, while both the velocity and velocity ratios are different. Given that the velocity and momentum ratios in case 1 match with those of D10 and D11, respectively, it is expected that the temperature profile in case 1 lies near those of D10–D12.²³ Note that the axial velocity in case 1 is about ten times that of the experiments (for the sake of computational efficiency), so the numerical data for comparison was extracted at an axial location about ten times farther downstream ($2.8 d_i$). The present result shows close agreement with experiment, especially in the inner jet region. Slight deviation may come from uncertainty in the experimental measurements due to probe-induced local flow disturbance and uncertainty in the setup of numerical boundary conditions.

At near- and supercritical pressures, the central dark core length was found to follow a functional relation with the momentum flux (M) ratio of A/M^n . The constants $A \in$,^{5,12} $n = 0.5$ were developed from the experimental data by Davis and Cherhoudi²³ and $A = 7.3$, $n = 0.58$ were found by Leyva *et al.*⁵⁶ Because the dark core

length is generally determined through an integrated shadowgraph image, it is hard to identify an exact length with the averaged density or temperature profile. In the present work, therefore, we propose that the dark core length is measured where the density along the inner jet centerline is almost asymptotic. As illustrated in Fig. 11, the actual

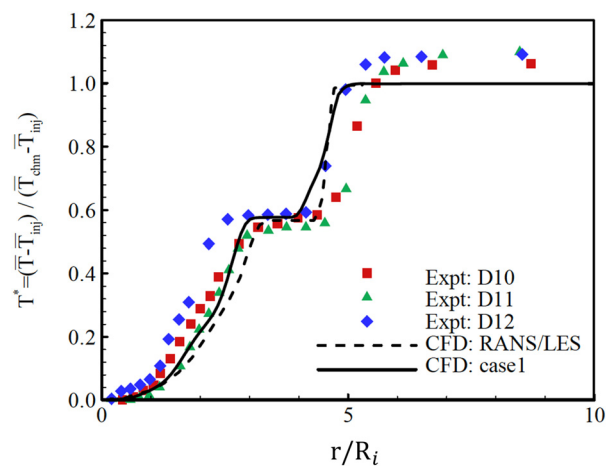


FIG. 10. Mean temperature radial profile: comparison with experiment and previous numerical results (Expt.: D10, D11, and D12 from Ref. 23; Computational fluid dynamics (CFD): RANS/LES from Ref. 55).

TABLE II. Operating conditions for mean temperature comparison.

	Expt.: D10	Expt.: D11	Expt.: D12	RANS/LES ⁵⁵	Case 1
P_{chm} (MPa)	4.95	4.94	4.94	4.95	4.94
T_{chm} (K)	237	228	233	237	233
T_f (K)	190	185	191	190	191
T_o (K)	129	133	132	129	132
u_f (m/s)	10.9	16.8	22.5	10.9	120
u_o (m/s)	3.0	3.9	3.6	3.0	32
u_f/u_o	3.6	4.3	6.3	3.6	3.75
$(\rho u^2)_f/(\rho u^2)_o$	2.7	5.1	9.6	2.7	3.44
Reference	Davis and Chehroudi ²³			Hosangadi <i>et al.</i> ⁵⁵	Current work

density distributions are represented by solid lines with symbols and the power-fit curve-fitting profiles are denoted by dashed-dotted lines. The end of the dark core can be located at the points where these two lines become bifurcated. The bottom plot in Fig. 11 shows the extracted dark core length along with empirical formula derived from

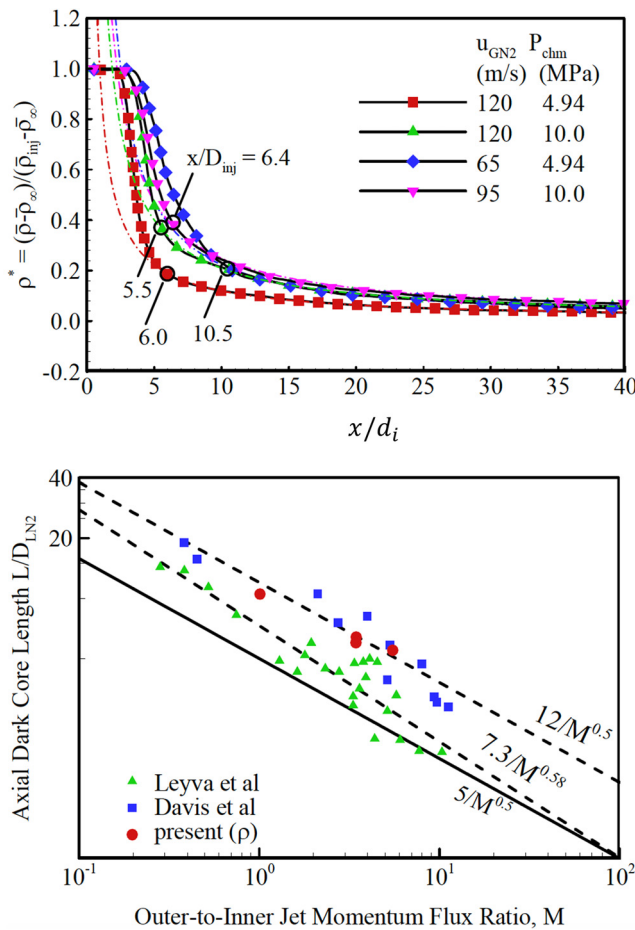


FIG. 11. Density profiles on the centerline (top) and extracted dark core length as function of momentum flux ratio (bottom).

the experimental data.^{23,56} The present result fits well with the empirical formula.

Figure 12 shows the outer-jet spreading angle of the present cases with analytical predictions and experimental data.^{56,57} The initial spreading angle is measured by starting from the point where the jet starts to grow to $10 d_i$. Using the same shear-coaxial jet injector configuration, good agreement is shown between the present simulation results and experimental data provided by Leyva *et al.*⁵⁶ and Rodriguez *et al.*⁵⁷ The spreading angle is much smaller than that predicted from the theoretical formula and other studies^{58–61} because of the appearance of a recirculation zone in the present study.

At a higher outer-to-inner velocity ratio, the inner potential core length is shorter because large-scale vortices pinch the centerline earlier. For a more quantitative measure, normalized axial velocities along the inner and outer jet centerlines are plotted in Fig. 13, where \bar{u}_∞ , \bar{u}_{inj1} , and \bar{u}_{inj2} represent the axial velocity in the far field, at the centers of the inner and outer jet exits, respectively. The axial coordinate is

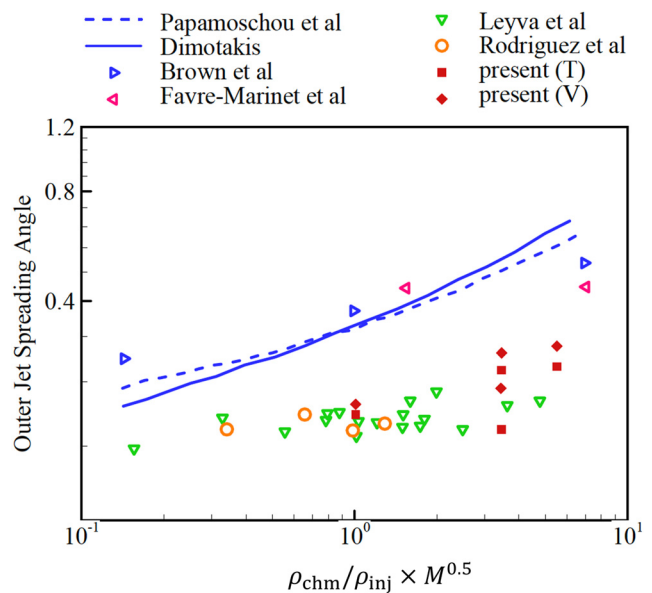


FIG. 12. Outward spreading angle: present results and from the literature.

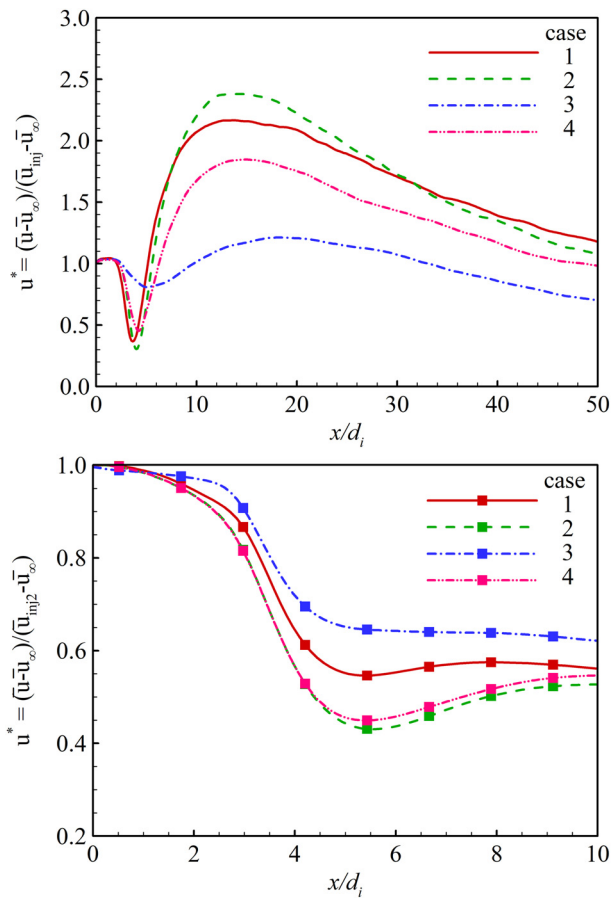


FIG. 13. Axial profiles of normalized axial velocity along centerlines of inner (top) and outer (bottom) jets.

normalized by the inner jet diameter d_i . Like those found by Balarac *et al.*⁶² in incompressible shear-coaxial jets, the mean axial velocity along the inner jet centerline remains constant to a certain distance, representing the inner potential core region. Due to the appearance of the low-pressure region between the inner and annular jets, the outer potential core bends in the centripetal direction; the radius of the coaxial jet is compressed and ambient fluid replaces the vacancy. As a result, the mean axial velocity along the outer jet centerline decreases fast, rather than remaining constant as expected by Balarac *et al.*⁶² The constriction of the outer jet can also be demonstrated by looking back into the isosurfaces of instantaneous temperature at 192 K, as shown in Fig. 5 and the streamlines in Fig. 8. Along the inner centerline, the mean axial velocity begins to decrease after passing the constant-value region, until the inner cold jet is well mixed with the annular warmer jet and the velocity begins to increase due to the traction from entrained fluid with higher velocity. Further downstream, the velocity will decrease again, after the component shear-coaxial jets become one single jet and that jet approaches its fully developed region. Another phenomenon worthy of mention is that the length of the inner potential core, represented by the points with lowest mean axial velocity along the inner jet centerline, increases with decreasing outer-to-inner

velocity ratio and ambient pressure. This echoes the discussion of Fig. 6 regarding the inner potential core.

Figure 14 presents the effects of pressure and velocity ratios on the axial profiles of normalized temperature, density, and compressibility factors along the inner- and outer-jet centerlines. These properties remain almost constant along both inner and outer centerlines immediately downstream of the injector exit, implying the existence of potential cores. Further downstream, evidently, the temperature decreases relatively slowly with a lower ambient pressure. These phenomena can be attributed to real-fluid critical divergence and lower thermal conductivity.¹⁰ A faster decrease in density is found along the inner jet centerline with a lower chamber pressure, due to a monotonic decrease in compressibility factor on the low-temperature regime and a faster increase in compressibility factor across the inflection point closer to

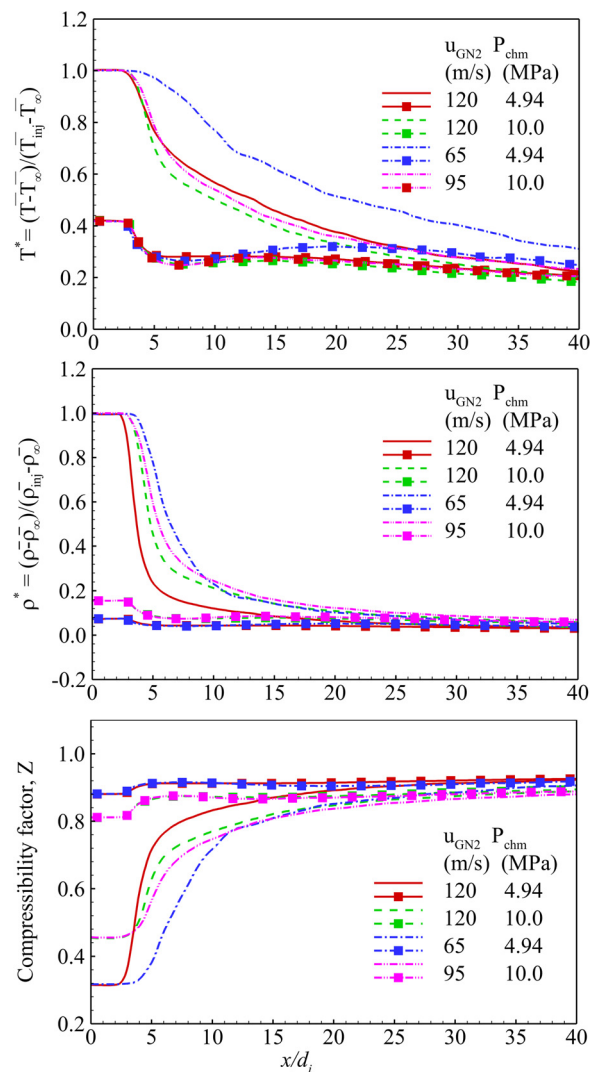


FIG. 14. Axial profiles of normalized temperature, density, and compressibility factor along inner (lines) and outer (lines with symbols) jet centerlines.

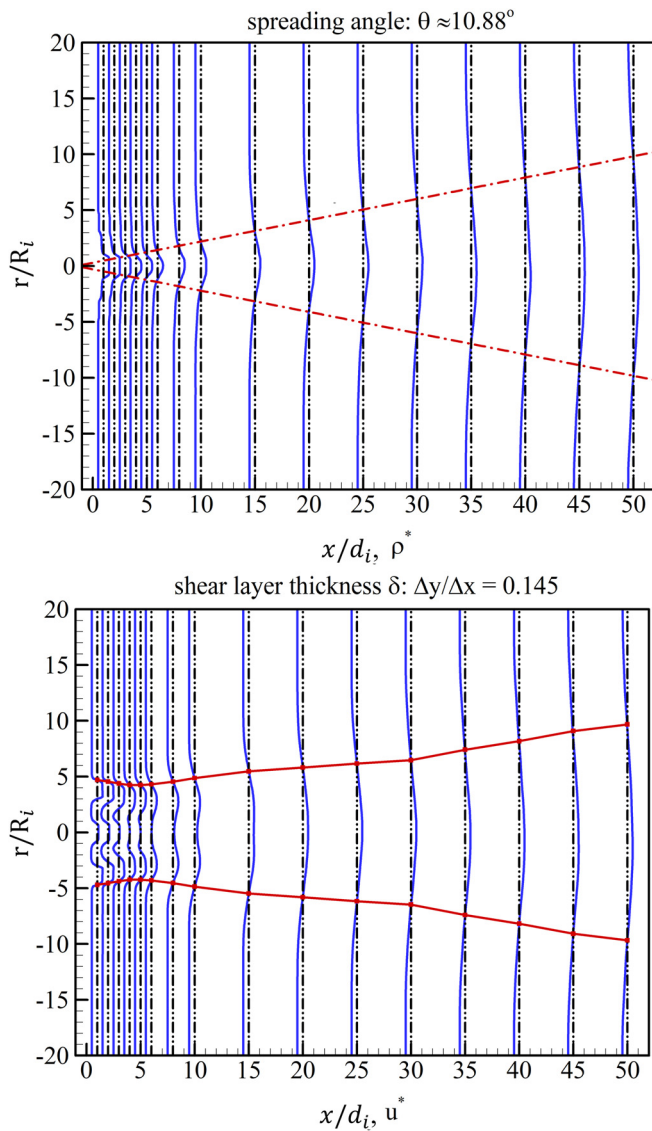


FIG. 15. Radial profiles of normalized mean density and axial velocity at various axial locations in case 3.

critical pressure. With a higher annular velocity, the normalized temperature and density decrease relatively faster, due to earlier entrainment of warmer fluids into the inner cold fluid region.

The radial distributions of normalized mean density and axial velocity at various axial locations are presented in Fig. 15, providing a straightforward illustration on how mean flow properties change when passing through the initial potential core, the transition zone, and the final fully developed self-similar region. In the initial potential core region, both the inner and outer jets behave like a single jet, with regular growth of shear layers. After the mean flow passes the transition zone, flow properties become self-similar. The normalized density is defined as $\rho^* = (\bar{\rho} - \bar{\rho}_\infty) / (\bar{\rho}_c - \bar{\rho}_\infty)$, with $\bar{\rho}_c$ representing the density at the inner centerline. The full width of the radial profile is

measured where the flow property of concern (density in the present figure) is one half of its maximum value $r_{1/2}$.

The red dot-dash lines that pass through all these $r_{1/2}$ represent the spreading angle of the turbulent shear-coaxial jet. In case 3, the spreading angle is about 10.88° . Under the same chamber pressure, the angle is found to be larger, with a higher outer-to-inner velocity ratio; with the same velocity ratio, the angle becomes smaller under a higher ambient pressure (see Fig. 16). The pressure effect is easily illustrated by considering a single jet injection: as the density ratio between ambient fluids and the single jet decreases, the jet will become flat and result in a narrower spreading angle. The normalized density distributions shown in Fig. 14 shows that case 2 has smaller $\bar{\rho}_\infty / \bar{\rho}$ than case 1. In order to allocate the shear layer thickness δ , a normalized velocity $u^* = \bar{u} / \bar{u}_{x,\max}$ recommended by Silva *et al.*⁶³ is introduced. In the definition, $\bar{u}_{x,\max}$ denotes the maximum mean axial velocity along the radial profile at specific axial locations x/D_{inj} . The shear-layer thickness is measured by the criterion that u^* equals to 0.5. As seen in Fig. 15, the resulting shear-coaxial thickness first decreases slightly for a certain distance, then begins to increase slowly in the transition region, and finally follows a linear increase. This trend is the same as that found by Silva *et al.*⁶³

C. Power spectral analysis

Power spectral analysis was conducted to provide more insight into the dominant frequencies of different dynamic events in the flow-field. Figure 17 shows the power spectral densities (PSD) of the pressure oscillation at eight different locations covering the entire flow region in case 1. Two dominant frequencies, 18.6 and 29.2 kHz, are found at probes 1, 4, and 7. Probes 2 and 5 represent the nearest location where only the dominant frequency 29.2 exists along the centerlines probes 3 and 6 represent the nearest location where the dominant frequency becomes inconspicuous. The frequency 18.6 kHz suggests the oscillation frequency of the flow recirculation region attached to the post-tip, which influences the flowfield only in the near-field region. The frequency 29.2 kHz, generated by the shear-layer instability, is related to the vortex shedding frequency. The same phenomena have been found for all other cases, with the vortex

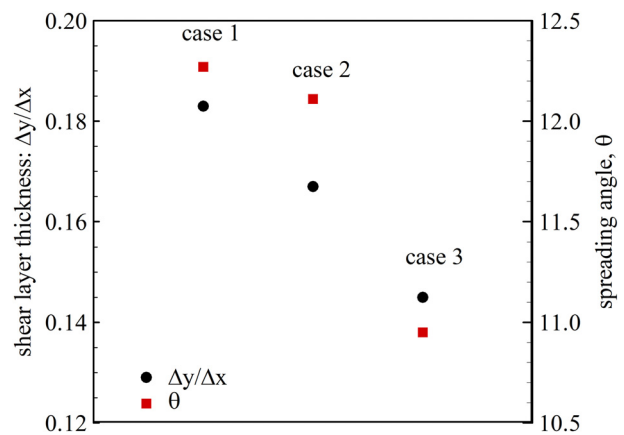


FIG. 16. Slope of shear-layer thickness and spreading angle in cases 1–4.

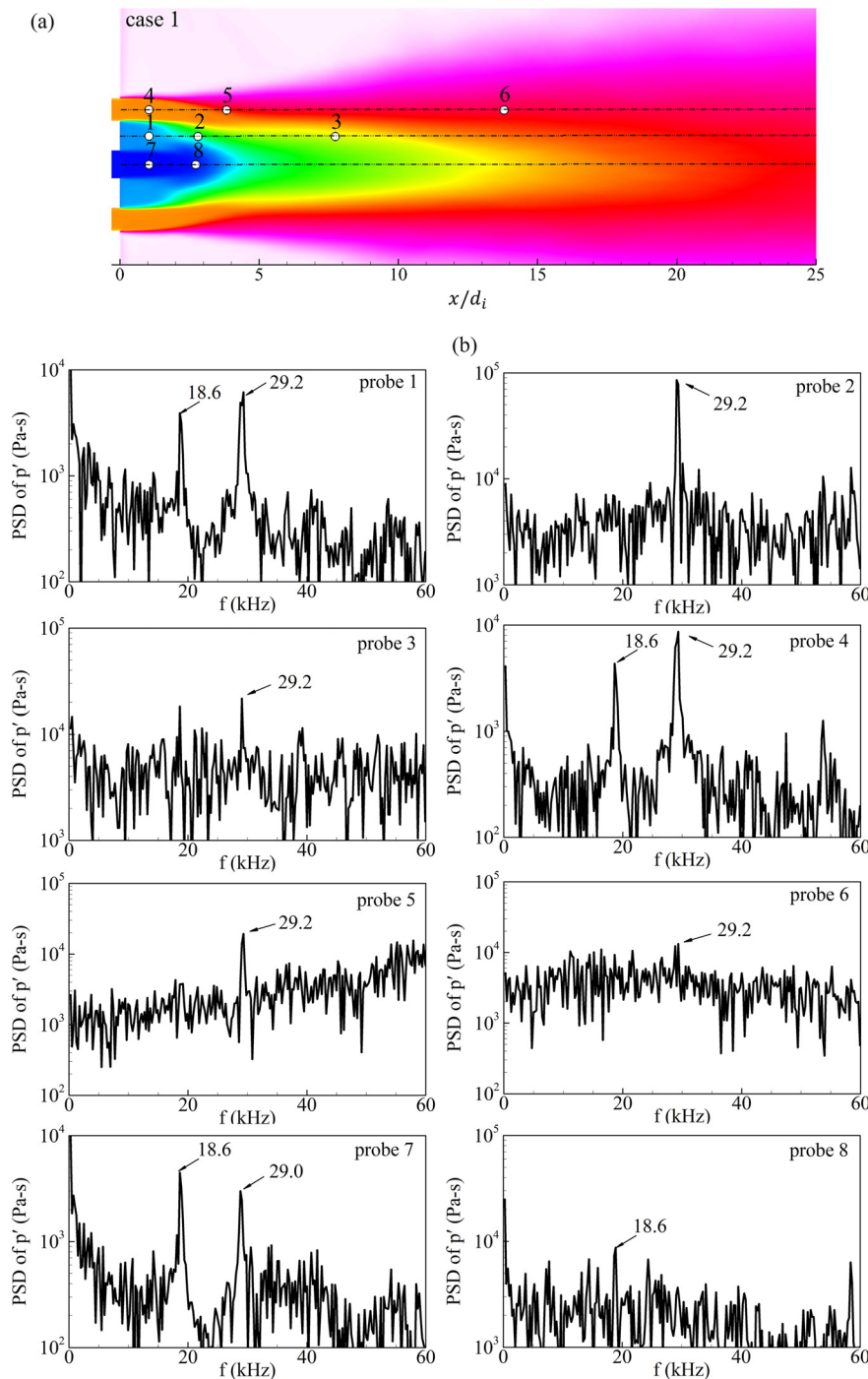


FIG. 17. (a) Probe locations; (b) corresponding power spectral densities of pressure oscillations.

shedding frequency becoming larger for case 2 and smaller for case 3. This trend is consistent with that found by using linear stability analysis on cryogenic nitrogen jets: the most unstable frequency increases with velocity ratio and ambient pressure.⁶⁴ The corresponding Strouhal number in case 3 is 0.421, determined from the

relationship $St = fL/\bar{U}$, where the characteristic length scale L is the radius of the outer tube and \bar{U} the difference between the outer and inner axial velocities. This Strouhal number is for the preferred mode and falls in the range of 0.25–0.5 according to Schadow and Gutmark.⁶⁵

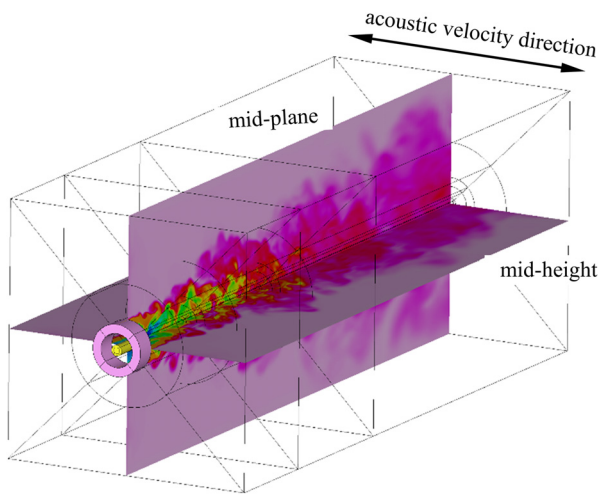


FIG. 18. Schematic diagram showing the chamber mid-height, mid-plane, and acoustic velocity direction.

D. Effect of acoustic modulation

The effect of transverse acoustic modulation on the flow dynamics of the shear-coaxial jet is explored in case 5. A sinusoidal pressure oscillation with a magnitude of 15 kPa and frequency 3 kHz is imposed

at one of the side walls at the radial boundary after the flow field is fully developed. The magnitude of pressure oscillation is nearly negligible, as compared to the ambient pressure level. Note that 3 kHz is not exactly the natural frequency of the downstream chamber, because of the dense-fluid effect in the inner jet region.

Figure 18 shows a schematic of the computational domain, illustrating the mid-height-plane and mid-plane, and acoustic velocity direction. The power spectral densities of the pressure and velocity oscillation near the opposite sidewall were calculated. The resultant dominant frequency of 3 kHz is identical to the frequency of the externally imposed oscillations, confirming the success of the acoustic excitation.

Figure 19 shows the temporal evolution of the temperature field in the mid-height section over one cycle of oscillation. A very small amplitude acoustic excitation modifies the injector fluid dynamics substantially. Large-scale sinusoidal structures in the mid-height direction parallel to the propagation of acoustic wave are clearly shown. Figure 20 presents snapshots of the temperature field without and with acoustic modulation. No obvious sinusoidal structure is seen in the mid-plane, which is perpendicular to the direction of acoustic propagation. In the mid-height plane, the acoustic modulation causes transverse displacement of the central liquid jet into the high-speed annular jet area. The dense fluid away from the centerline is accelerated in the axial direction by the annulus flow. The resultant impact on the coaxial jet induces a cusp-shaped structure, which significantly improves the mixing and heat transfer between the inner and outer jet fluid.

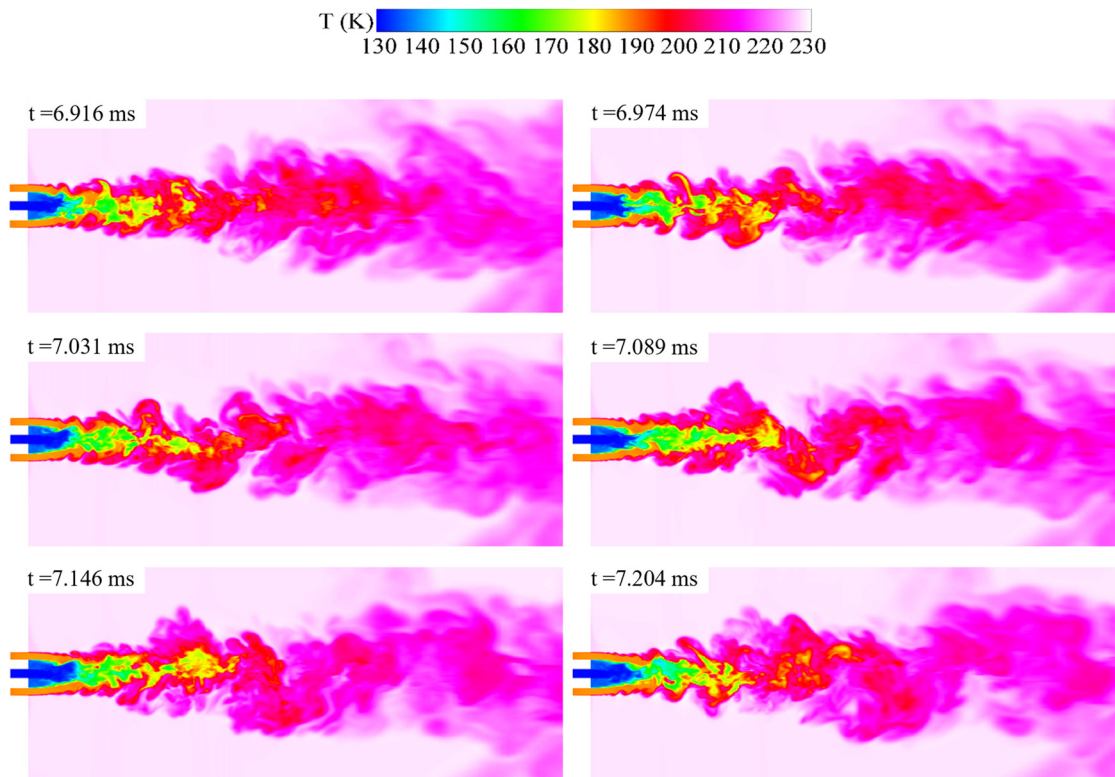


FIG. 19. Snapshots of temperature field in the mid-height section in case 5.

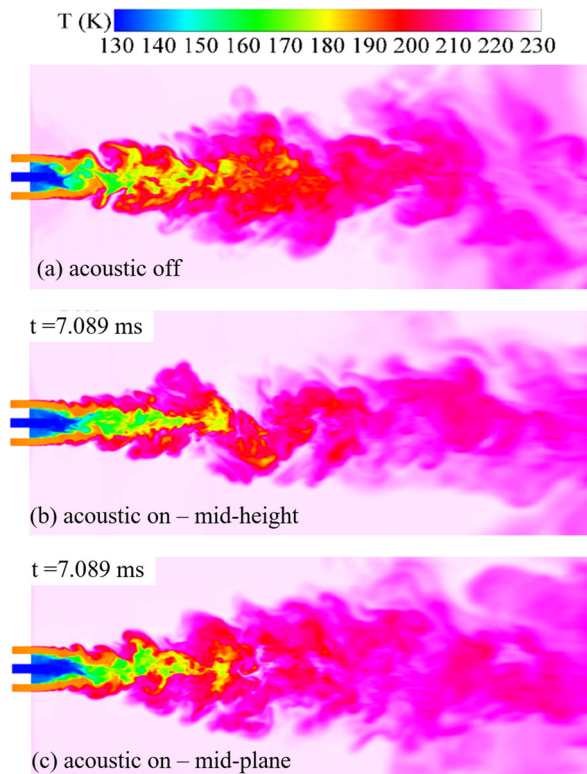


FIG. 20. Snapshots of temperature field (a) without acoustic field; (b) with acoustic field (mid-height section); (c) with acoustic field (mid-plane section).

V. CONCLUSION

Large-eddy simulations have been conducted to investigate shear-coaxial jet injection and mixing under supercritical pressures, with nitrogen as the working fluid. The numerical model accommodates full conservation laws, real-fluid thermodynamics, and transport phenomena over the entire fluid state of concern. The influences of ambient pressure, inner-to-outer velocity ratio, and acoustic modulation on the injector flow dynamics are systematically investigated.

The near-field injector flow dynamics are characterized by the development of three shear layers and the evolution of two potential cores. The outer shear layers prevail over the inner and impact the growth of the whole jet, due to the greater shear effects between the high-speed outer stream and the surroundings. Two counter-rotating recirculation regions are observed immediately downstream of the central post, oscillating at a frequency smaller than that of the dominant vortex shedding of the outer shear layer. Owing to the intensive fluid property variations in the flow field, a series of large density-gradient regions are formed around the jet surface, which significantly influences the injector flow dynamics. The dominant effects of the outer-to-inner velocity ratio on the flow evolution are demonstrated. As the injection velocity of the annular stream increases, turbulent mixing is greatly enhanced. As a result, the inner and outer potential cores are reduced, and the jet-spreading angle becomes wider. The influence of ambient pressure on the jet mixing and entrainment is also examined. An increase in ambient pressure gives rise to a shorter

inner potential core and a smaller jet spread angle. The predicted dark core length and outer spreading angle show good agreement with previous experimental results. The introduction of transverse acoustic excitation induces large sinusoidal oscillations of the inner dense-fluid stream along the direction of acoustic motion and promotes the mixing of the inner and outer streams.

ACKNOWLEDGMENTS

This work was sponsored partly by the Air Force Office of Scientific Research, Grant No. FA9550-04-1-0014, partly by the John L. and Genevieve H. McCain Endowment at the Pennsylvania State University, and the Ralph N. Read Endowment at the Georgia Institute of Technology. The authors gratefully acknowledge the support of Dr. Mitat A. Birkan.

DATA AVAILABILITY

The data that support the findings of this study are available from the corresponding author upon reasonable request.

REFERENCES

- ¹Liquid Rocket Engine Combustion Instability, Progress in Aeronautics and Astronautics, edited by W. E. Anderson and V. Yang (AIAA, 1995), Vol. 169.
- ²J. C. Oefelein and V. Yang, "Modeling high-pressure mixing and combustion processes in liquid rocket engines," *J. Propul. Power* **14**(5), 843–857 (1998).
- ³V. Yang, "Modeling of supercritical vaporization, mixing, and combustion processes in liquid-fueled propulsion systems," *Proc. Combust. Inst.* **28**(1), 925–942 (2000).
- ⁴M. Oschwald and A. Schik, "Supercritical nitrogen free jet investigated by spontaneous Raman scattering," *Exp. Fluids* **27**(6), 497–506 (1999).
- ⁵M. Oschwald, "Spreading angle and centerline variation of density of supercritical nitrogen jets," *Atomization Sprays* **12**(1–3), 91–106 (2002).
- ⁶B. Chehroudi, D. Talley, and E. Coy, "Visual characteristics and initial growth rates of round cryogenic jets at subcritical and supercritical pressures," *Phys. Fluids* **14**(2), 850–861 (2002).
- ⁷R. Branam and W. Mayer, "Characterization of cryogenic injection at supercritical pressure," *J. Propul. Power* **19**(3), 342–355 (2003).
- ⁸C. Segal and S. Polikhov, "Subcritical to supercritical mixing," *Phys. Fluids* **20**(5), 052101 (2008). No.
- ⁹N. Zong and V. Yang, "Cryogenic fluid jets and mixing layers in transcritical and supercritical environments," *Combust. Sci. Technol.* **178**(1–3), 193–227 (2006).
- ¹⁰N. Zong, H. Meng, S.-Y. Hsieh, and V. Yang, "A numerical study of cryogenic fluid injection and mixing under supercritical conditions," *Phys. Fluids* **16**(12), 4248–4261 (2004).
- ¹¹T. Schmitt, L. Selle, A. Ruiz, and B. Cuenot, "Large-eddy simulation of supercritical-pressure round jets," *AIAA J.* **48**(9), 2133–2144 (2010).
- ¹²R. N. Dahms and J. C. Oefelein, "Liquid jet breakup regimes at supercritical pressures," *Combust. Flame* **162**(10), 3648–3657 (2015).
- ¹³C. Muthukumar and A. Vaidyanathan, "Experimental study of elliptical jet from supercritical to subcritical conditions using planar laser induced fluorescence," *Phys. Fluids* **27**(3), 034109 (2015).
- ¹⁴S. DeSouza and C. Segal, "Sub- and supercritical jet disintegration," *Phys. Fluids* **29**(4), 047107 (2017).
- ¹⁵W. Mayer and H. Tamura, "Propellant injection in a liquid oxygen/gaseous hydrogen rocket engine," *J. Propul. Power* **12**(6), 1137–1147 (1996).
- ¹⁶W. O. Mayer, A. H. Schik, B. Vielle, C. Chauveau, I. Gokalp, D. G. Talley, and R. D. Woodward, "Atomization and breakup of cryogenic propellants under high-pressure subcritical and supercritical conditions," *J. Propul. Power* **14**(5), 835–842 (1998).
- ¹⁷S. Candel, G. Herding, R. Synder, P. Scoufflaire, C. Rolon, L. Vingert, M. Habiballah, F. Grisch, M. Péalat, and P. Bouchardy, "Experimental investigation of shear coaxial cryogenic jet flames," *J. Propul. Power* **14**(5), 826–834 (1998).

- ¹⁸G. Singla, P. Scoufflaire, C. Rolon, and S. Candel, "Transcritical oxygen/transcritical or supercritical methane combustion," *Proc. Combust. Inst.* **30**(2), 2921–2928 (2005).
- ¹⁹S. Candel, M. Juniper, G. Singla, P. Scoufflaire, and C. Rolon, "Structure and dynamics of cryogenic flames at supercritical pressure," *Combust. Sci. Technol.* **178**(1–3), 161–192 (2006).
- ²⁰J. Lux and O. Haidn, "Effect of recess in high-pressure liquid oxygen/methane coaxial injection and combustion," *J. Propul. Power* **25**(1), 24–32 (2009).
- ²¹J. Lux and O. Haidn, "Flame stabilization in high-pressure liquid oxygen/methane rocket engine combustion," *J. Propul. Power* **25**(1), 15–23 (2009).
- ²²D. Davis and B. Chehroudi, "The effects of pressure and acoustic field on a cryogenic coaxial jet," AIAA Paper No. 2004-1330, 2004.
- ²³D. W. Davis and B. Chehroudi, "Measurements in an acoustically driven coaxial jet under sub-, near-, and supercritical conditions," *J. Propul. Power* **23**(2), 364–374 (2007).
- ²⁴J. C. Oefelein, "Thermophysical characteristics of shear-coaxial LOX-H₂ flames at supercritical pressure," *Proc. Combust. Inst.* **30**(2), 2929–2937 (2005).
- ²⁵J. C. Oefelein, "Mixing and combustion of cryogenic oxygen-hydrogen shear-coaxial jet flames at supercritical pressure," *Combust. Sci. Technol.* **178**(1–3), 229–252 (2006).
- ²⁶N. Zong and V. Yang, "Near-field flow and flame dynamics of LOX/methane shear-coaxial injector under supercritical conditions," *Proc. Combust. Inst.* **31**(2), 2309–2317 (2007).
- ²⁷M. Masquelet and S. Menon, "Large-eddy simulation of flame-turbulence interactions in a shear coaxial injector," *J. Propul. Power* **26**(5), 924–935 (2010).
- ²⁸T. Schmitt, Y. Méry, M. Boileau, and S. Candel, "Large-eddy simulation of oxygen/methane flames under transcritical conditions," *Proc. Combust. Inst.* **33**(1), 1383–1390 (2011).
- ²⁹T. Kim, Y. Kim, and S.-K. Kim, "Effects of pressure and inlet temperature on coaxial gaseous methane/liquid oxygen turbulent jet flame under transcritical conditions," *J. Supercrit. Fluids* **81**, 164–174 (2013).
- ³⁰L. Hakim, A. Ruiz, T. Schmitt, M. Boileau, G. Staffelbach, S. Ducruix, B. Cuenot, and S. Candel, "Large eddy simulations of multiple transcritical coaxial flames submitted to a high-frequency transverse acoustic modulation," *Proc. Combust. Inst.* **35**(2), 1461–1468 (2015).
- ³¹A. Urbano, L. Selle, G. Staffelbach, B. Cuenot, T. Schmitt, S. Ducruix, and S. Candel, "Exploration of combustion instability triggering using large eddy simulation of a multiple injector liquid rocket engine," *Combust. Flame* **169**, 129–140 (2016).
- ³²P. E. Lapenna, P. P. Ciottoli, and F. Creta, "Unsteady non-premixed methane/oxygen flame structures at supercritical pressures," *Combust. Sci. Technol.* **189**(12), 2056–2082 (2017).
- ³³T. Schmitt, J. Rodriguez, I. Leyva, and S. Candel, "Experiments and numerical simulation of mixing under supercritical conditions," *Phys. Fluids* **24**(5), 055104 (2012).
- ³⁴J. Bellan, "Supercritical (and subcritical) fluid behavior and modeling: Drops, streams, shear and mixing layers, jets and sprays," *Prog. Energy Combust. Sci.* **26**(4–6), 329–366 (2000).
- ³⁵J. C. Oefelein, "Large eddy simulation of turbulent combustion processes in propulsion and power systems," *Prog. Aerosp. Sci.* **42**(1), 2–37 (2006).
- ³⁶H. Terashima and M. Koshi, "Approach for simulating gas-liquid-like flows under supercritical pressures using a high-order central differencing scheme," *J. Comput. Phys.* **231**(20), 6907–6923 (2012).
- ³⁷S. Kawai, H. Terashima, and H. Negishi, "A robust and accurate numerical method for transcritical turbulent flows at supercritical pressure with an arbitrary equation of state," *J. Comput. Phys.* **300**, 116–135 (2015).
- ³⁸H. Müller, C. A. Niedermeier, J. Matheis, M. Pfitzner, and S. Hickel, "Large-eddy simulation of nitrogen injection at trans- and supercritical conditions," *Phys. Fluids* **28**(1), 015102 (2016).
- ³⁹P. C. Ma, Y. Lv, and M. Ihme, "An entropy-stable hybrid scheme for simulations of transcritical real-fluid flows," *J. Comput. Phys.* **340**, 330–357 (2017).
- ⁴⁰X. Wang, H. Huo, U. Unnikrishnan, and V. Yang, "A systematic approach to high-fidelity modeling and efficient simulation of supercritical fluid mixing and combustion," *Combust. Flame* **195**, 203–215 (2018).
- ⁴¹B. Chehroudi, "Recent experimental efforts on high-pressure supercritical injection for liquid rockets and their implications," *Int. J. Aerosp. Eng.* **2012**, 1.
- ⁴²T. Liu, N. Zong, and V. Yang, "Dynamics of shear-coaxial cryogenic nitrogen jets with acoustic excitation under supercritical conditions," AIAA Paper 2006-759, 2006.
- ⁴³H. Huo and V. Yang, "Large-eddy simulation of supercritical combustion: Model validation against gaseous H₂-O₂ injector," *J. Propul. Power* **33**(5), 1272–1284 (2017).
- ⁴⁴G. Erlebacher, M. Y. Hussaini, C. G. Speziale, and T. A. Zang, "Toward the large-eddy simulation of compressible turbulent flows," *J. Fluid Mech.* **238**, 155–185 (1992).
- ⁴⁵G. Soave, "Equilibrium constants from a modified Redlich-Kwong equation of state," *Chem. Eng. Sci.* **27**(6), 1197–1203 (1972).
- ⁴⁶U. Unnikrishnan, H. Huo, X. Wang, and V. Yang, "Subgrid scale modeling considerations for large eddy simulation of supercritical turbulent mixing and combustion," *Phys. Fluids* (to be published).
- ⁴⁷S. Takahashi, "Preparation of a generalized chart for the diffusion coefficients of gases at high pressures," *J. Chem. Eng. Jpn.* **7**(6), 417–420 (1975).
- ⁴⁸H. Meng and V. Yang, "A unified treatment of general fluid thermodynamics and its application to a preconditioning scheme," *J. Comput. Phys.* **189**(1), 277–304 (2003).
- ⁴⁹R. C. Swanson and E. Turkel, "On central-difference and upwind schemes," *J. Comput. Phys.* **101**(2), 292–306 (1992).
- ⁵⁰D. T. Banuti and K. Hannemann, "The absence of a dense potential core in supercritical injection: A thermal break-up mechanism," *Phys. Fluids* **28**(3), 035103 (2016).
- ⁵¹Y. Dubief and F. Delcayre, "On coherent-vortex identification in turbulence," *J. Turbul.* **1**, 011 (2000).
- ⁵²G. Nastro, J. Fontane, and L. Joly, "Optimal perturbations in viscous round jets subject to Kelvin-Helmholtz instability," *J. Fluid Mech.* **900**, 1–25 (2020).
- ⁵³C. Arratia, C. Caulfield, and J.-M. Chomaz, "Transient perturbation growth in time-dependent mixing layers," *J. Fluid Mech.* **717**, 90 (2013).
- ⁵⁴H. Rehab, E. Villermaux, and E. Hopfinger, "Flow regimes of large-velocity-ratio coaxial jets," *J. Fluid Mech.* **345**, 357–381 (1997).
- ⁵⁵A. Hosangadi, C. Lee, C. Kannepalli, and S. Arunajatesan, "Three-dimensional hybrid RANS/LES simulations of a supercritical liquid nitrogen jet," AIAA Paper No. 2008-5227, 2008.
- ⁵⁶I. Leyva, B. Chehroudi, and D. Talley, "Dark core analysis of coaxial injectors at sub-, near-, and supercritical conditions in a transverse acoustic field," AIAA Paper No. 2007-5456, 2007.
- ⁵⁷J. Rodriguez, I. Leyva, B. Chehroudi, and D. Talley, "Results of subcritical one-phase coaxial jet spread angles and subcritical to supercritical acoustically-forced coaxial jet dark core lengths," AIAA Paper No. 2008-4561, 2008.
- ⁵⁸G. L. Brown and A. Roshko, "On density effects and large structure in turbulent mixing layers," *J. Fluid Mech.* **64**(4), 775–816 (1974).
- ⁵⁹P. E. Dimotakis, "Two-dimensional shear-layer entrainment," *AIAA J.* **24**(11), 1791–1796 (1986).
- ⁶⁰D. Papamoschou and A. Roshko, "The compressible turbulent shear layer: An experimental study," *J. Fluid Mech.* **197**, 453–477 (1988).
- ⁶¹M. Favre-Marinet and E. C. Schettini, "The density field of coaxial jets with large velocity ratio and large density differences," *Int. J. Heat Mass Transfer* **44**(10), 1913–1924 (2001).
- ⁶²G. Balarac, O. Métais, and M. Lesieur, "Mixing enhancement in coaxial jets through inflow forcing: A numerical study," *Phys. Fluids* **19**(7), 075102 (2007).
- ⁶³C. B. D. Silva, G. Balarac, and O. Métais, "Transition in high velocity ratio coaxial jets analysed from direct numerical simulations," *J. Turbul.* **4**(1), 024 (2003).
- ⁶⁴T. Liu, "Shear-coaxial injection and mixing of cryogenic fluids under supercritical conditions," Ph.D. thesis (The Pennsylvania State University, 2007).
- ⁶⁵K. Schadow and E. Gutmark, "Combustion instability related to vortex shedding in dump combustors and their passive control," *Prog. Energy Combust. Sci.* **18**(2), 117–132 (1992).